Contributions to Mineralogy and Petrology (2024) 179:23
https://doi.org/10.1007/s00410-024-02105-4

ORIGINAL PAPER

Vapor-phase crystallization from a hydrous silicate melt: an experimental simulation of diktytaxitic texture

Ryosuke Sakurai[1] · Michihiko Nakamura[2] · Satoshi Okumura[2] · Mayumi Mujin[2,3] · Takayuki Nakatani[4]

Received: 7 November 2023 / Accepted: 24 January 2024 / Published online: 6 March 2024

Abstract

Groundmass textures of volcanic rocks provide valuable insights into the processes of magma ascent, crystallization, and eruption. The diktytaxitic texture, characterized by a lath-shaped arrangement of feldspar microlites forming glass-free and angular pores, is commonly observed in silicic dome-forming rocks and Vulcanian ashfall deposits. This texture has the potential to control the explosivity of volcanic eruptions because its micropore network allows pervasive degassing during the final stages of magma ascent and eruption. However, the exact conditions and kinetics of the formation of diktytaxitic textures, which are often accompanied by vapor-phase cristobalite, remain largely unknown. Here, we show that the diktytaxitic texture and vapor-phase minerals, cristobalite and alkali feldspar, can be produced from bulk-andesitic magma with rhyolitic glass under water-saturated, near-solidus conditions (± ~10 MPa and ± ~20 °C within the solidus; 10–20 MPa and 850 °C for our starting pumices). Such crystallization proceeds through the partial evaporation of the supercooled melt, followed by the deposition of cristobalite and alkali feldspar as a result of the system selecting the fastest crystallization pathway with the lowest activation energy. The previously proposed mechanisms of halogen-induced corrosion or melt segregation by gas-driven filter pressing are not particularly necessary, although they may occur concurrently. Diktytaxitic groundmass formation is completed within 4–8 days, irrespective of the presence or composition of the halogen. These findings constrain the outgassing of lava domes and shallow magma intrusions and provide new insights into the final stages of hydrous magma crystallization on Earth.

Keywords Crystallization experiment · Evaporation–deposition · Cristobalite · Diktytaxitic texture · Lava dome

Introduction

The textures of volcanic rocks represent magmatic processes, such as magma storage, ascent, and eruption. The groundmass texture of volcanic rocks records late-stage crystallization and degassing. The groundmass of volcanic necks and lava domes often show a diktytaxitic texture characterized by a lath-shaped arrangement of feldspar microlites, forming glass-free and angular pores. Volcanic ashes and lava fragments from Vulcanian explosions and ash plumes also contain diktytaxitic groundmass (e.g., Pallister et al. 2008; Horwell et al. 2013; Gaunt et al. 2016; Kushnir et al. 2016; Schipper et al. 2017; Ikegami et al. 2018). The interconnected micropores in the diktytaxitic groundmass suggest their critical role in facilitating gas escape during the final stage of magma emplacement, thus controlling eruption explosivity and volcanic hazards such as pyroclastic density currents and Vulcanian explosions (e.g., Sparks 1997; Cassidy et al. 2018; Kushnir et al. 2016).

Communicated by Othmar Müntener.

✉ Ryosuke Sakurai
sakurai@eps.s.u-tokyo.ac.jp

[1] Department of Earth and Planetary Science, Graduate School of Science, The University of Tokyo, Tokyo 113-0033, Japan

[2] Department of Earth Science, Graduate School of Science, Tohoku University, Sendai 980-8578, Japan

[3] Section of Natural Science, Division of Developmental Research in Education Programs, Institute for Excellence in Higher Education, Tohoku University, Sendai 980-8576, Japan

[4] Geological Survey of Japan, National Institute of Advanced Industrial Science and Technology (AIST), Tsukuba 305-8567, Japan

Another feature of interest is the common association between the diktytaxitic texture and vapor-phase (pneumatolytic) high-temperature silica polymorphs, such as cristobalite (e.g., Baxter et al. 1999; Pallister et al. 2008; Horwell et al. 2013; Kushnir et al. 2016; Schipper et al. 2015, 2017, 2020; Ikegami et al. 2018) and tridymite (Pallister et al. 2008; Horwell et al. 2013). The simultaneous formation of high-temperature silica polymorphs in the presence of high-temperature volcanic gas provides clues to their formation mechanisms. Volcanic ash from continuously erupting volcanoes often contains significant quantities of cristobalite crystals (e.g., Baxter et al. 1999; Horwell et al. 2003; Hillman et al. 2012), which can cause a lung disease known as silicosis and lead to increased mortality associated with lung cancer when inhaled into the respiratory tract (Higuchi et al. 2012; Sato et al. 2018). Therefore, an understanding of the formation mechanisms of vapor-phase cristobalite is critical for assessing health hazards.

Although diktytaxitic texture has long been recognized in petrographic literature (e.g., Fuller 1931), its formation conditions and mechanisms remain elusive. Two possible formation mechanisms of diktytaxitic textures accompanied by cristobalite have been proposed: melt segregation by gas-driven filter pressing (Peck 1978; Anderson et al. 1984; Bacon 1986; Sanders 1986; Goff 1996; Sisson and Bacon 1999; Pistone et al. 2015, 2020) and melt or glass corrosion by halogen-bearing vapor (De Hoog et al. 2005; Horwell et al. 2013; Schipper et al. 2015, 2017, 2019; Yoshimura and Nakagawa 2021). Gas filter pressing is generally attributed to secondary boiling associated with rapid crystallization during the intrusion of mafic magma into a felsic host rock or a mash-like magma chamber. This is evidenced by the occurrence of diktytaxitic textures in mafic inclusions and vitrified melt in vesicles of the host rock, which is chemically related to the intrusive magma (Peck 1978; Anderson et al. 1984; Bacon 1986; Sanders 1986; Goff 1996; Sisson and Bacon 1999). However, detailed conditions such as temperature, pressure, ambient gas composition, and time for the formation of diktytaxitic texture remain uncertain. Pistone et al. (2020) demonstrated through laboratory experiments that the segregation of melt due to filter presses during the crystallization of felsic magma is increased closer to its solidus temperature. Despite the potential insights offered by diktytaxitic textures and vapor-phase silica, the formation of these features has yet to be thoroughly studied under controlled laboratory conditions. In this study, crystallization experiments on hydrous melts were performed under vapor-saturation conditions to elucidate the conditions and kinetics of the formation of diktytaxitic texture. The potential role of halogens in this process was also investigated in HCl- and HF-bearing systems.

Methods

Preparation of starting materials and capsules

As starting materials for the hydrothermal experiments, we used two andesitic pumice clasts, SAK-W and SAK-E, from the 1914 (Taisho) Plinian eruption of Sakurajima volcano, Kagoshima Prefecture, Kyushu, Japan. Since its most recent large eruption in 1914–1915, where the VEI 4 Plinian eruption was followed by a lava flow of 1.54 km^3 (in dense rock equivalent), the Sakurajima volcano has experienced repeated Vulcanian explosions > 1000 times/y at its most active phase, interpolated with ash plumes, and rarely with Strombolian eruptions. Diktytaxitic particles and cristobalite are common in volcanic ash (Hillman et al. 2012; Matsumoto et al. 2013). Residents near the neighborhood have long suffered from respiratory illnesses caused by volcanic ash (Hillman et al. 2012; Higuchi et al. 2012). Samples SAK-W and SAK-E were collected from the outcrops of Hakamagoshi and Nagasakibana, respectively, located on the western and eastern flanks of Sakurajima volcano. These two samples have almost the same bulk chemical composition (Table 1) but differ slightly in porosity (low in SAK-W) and microlite number density (high in SAK-W) (Fig. 1a and b). These two samples were selected for control experiments to investigate the effects of pre-existing groundmass crystals on nucleation during the experiments. The groundmass of SAK-W contains plagioclase and pyroxene microlites of 13.0–17.5 and 1.3–3.3 vol%, respectively, while SAK-E was almost microlite-free. All the pumice samples were carefully cut into cubes (approximately 1.5 mm) to avoid phenocrysts. One or two pumice cubes were placed in Au capsules with

Table 1 Bulk and glass chemical composition of the starting materials

	SAK-W		SAK-E	
	Bulk (wt.%)	Glass (wt.%)	Bulk (wt.%)[a]	Glass (wt.%)
SiO_2	62.31	72.54	62.68	69.86
TiO_2	0.80	0.85	0.81	0.78
Al_2O_3	16.77	12.65	16.57	13.92
FeO	6.13	3.96	6.09	4.28
MnO	0.15	0.05	0.14	0.07
MgO	2.28	0.57	2.25	0.89
CaO	6.02	2.20	5.65	3.25
Na_2O	3.52	4.01	3.82	4.17
K_2O	1.81	2.84	1.84	2.48
P_2O_5	0.21	0.32	0.16	0.30
Total[b]	100.00	100.00	100.00	100.00

[a]After Otsuki et al. (2015)

[b]Normalized to volatile-free 100%

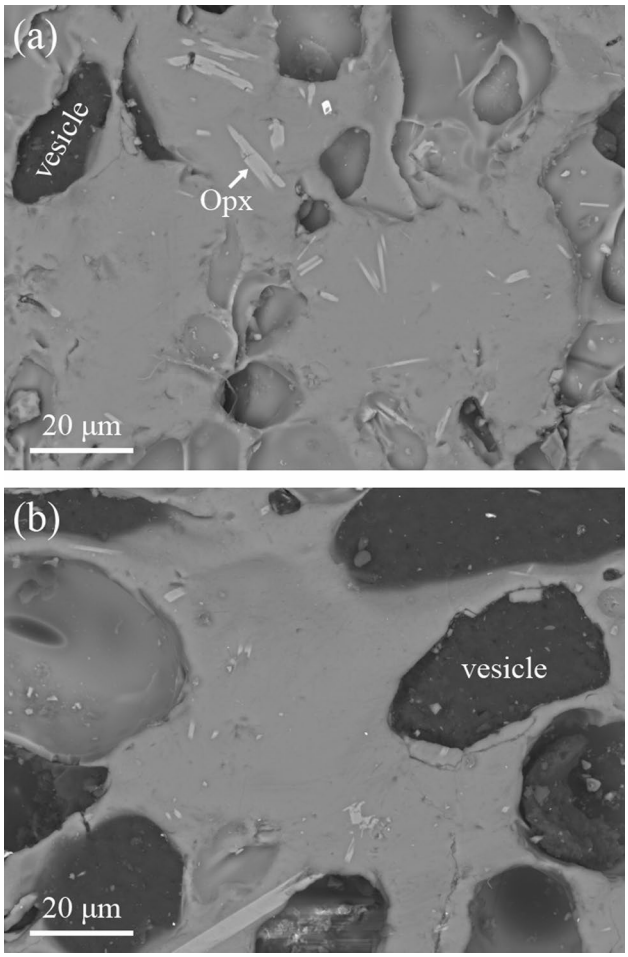

Fig. 1 Backscattered electron images of polished cross-sections of two pumice clasts used as the starting materials for the hydrothermal experiments. **a** SAK-W and **b** SAK-E. Bright elongated crystals are orthopyroxene (Opx) and the dark areas are resin-filled original vesicles

sufficient water to ensure saturation under the target pressure and temperature (*P*–*T*) conditions. HCl or HF was added as a 1000 ppm water solution in some capsules.

Hydrothermal experiments

All experiments were conducted using cold-seal pressure vessels made of Rene 41 or Inconel 713LC, which were aged under hydrothermal conditions to form oxide films. Water was used as the pressure medium and was expected to become a supercritical fluid only in Run# PLT12 because of the relatively high pressure, which exceeded its critical point. Water was present as vapor in the other runs. Capsules were supported by nickel filler rods. Hydrogen transport through the Au capsule allowed the redox environment inside the capsule to be buffered by the surrounding metals, maintaining an oxygen fugacity approximately equal to that of nickel–nickel oxide (NNO) buffer, within a range of ± 0 to + 1 in logarithmic scale (Okumura et al. 2021).

All the experiments were conducted under isobaric–isothermal conditions at 2.5–80 MPa and 750–950 °C. The pumice cubes and deionized distilled water were placed in Au capsules with 3.0 and 2.7 mm outer and inner diameters, respectively, and welded together. The Au capsule was then heated from room temperature to the target temperature *T* (°C) for approximately 1 h, maintained for the desired duration, *t* (6–189 h), and quenched by introducing the capsule into a cooling tube or cooling the pressure vessel with compressed air and water. The experimental pressure was maintained manually or by using an automatic syringe pumping system during each experiment. Table 2 summarizes the operating conditions. The weight-based water–rock ratio *u* was calculated from the pumice weight and weight gain after the addition of water. The experimental condition for PLT02A ($u = 13.0$ wt.%, $P = 10$ MPa, $T = 850$ °C, and $t = 189$ h) was defined as the reference condition for control experiments on water–rock ratio (2.6–13.0 and > 100 wt.%; Water-*u* series), pressure (2.5–80 MPa; Water-*P* series), temperature (750–950 °C; Water-*T* series), and run duration (6–384 h; Water-*t* series). For Run# PLT16, one end of the capsule was crimped without welding to expose the pumice cubes to the large volume of water vapor that filled the vessel as a pressure medium. The capsules containing $HCl_{(aq)}$ or $HF_{(aq)}$ were heated at 10 MPa and 850 °C for 6–189 h (HCl-*t* and HF-*t* series). The experiments were started immediately after preparing these capsules to minimize the corrosion of the pumice cubes using liquid HCl or HF solution. For the experimental series other than the Water-*u*, the water–rock ratio varied between experiments in the range of 3.4–27.4 wt.%.

Sample analysis

The recovered Au capsules were carefully opened to prevent damage. The surface textures of the run products and internal walls of Au capsules were observed using a field-emission scanning electron microscope (FE-SEM; JEOL JSM-7100F). Subsequently, the run products were embedded in epoxy resin, polished to expose the cross-section, and coated with carbon. The chemical compositions of minerals and residual glass of run products were analyzed on polished sections using energy dispersive X-ray spectroscopy (EDS; JEOL JED-2300F) under analytical conditions of a 1 nA beam current and 15 kV accelerating voltage with the ZAF (effects of atomic number (Z), absorption (A), and fluorescence excitation (F)) correction. The concentrations of major elements (Si, Ti, Al, Fe, Mn, Mg, Ca, Na, K, and P) of silica minerals (6–13 pcs/sample), feldspar microlites (12–27 pcs/sample), and pyroxene microlites (12–23 pcs/sample) were analyzed. The major element concentrations of glass in the

Table 2 Experimental conditions and presence of cristobalite and alkali feldspar

Series	Run#	Encapsulated liquid[a]	u_{H2O}[b] (wt%)	P[c] (MPa)	T[d] (°C)	t[e] (h)	Mineral presence[f]	
							Crs (> 10 μm)	Kfs
Water-*u*	PLT14A	Pure water	2.6	10	850	189	✓	✓
	PLT02B		5.1				✓	✓
	PLT02A[g]		13.0				✓	✓
	PLT16		> 100				✓	✓
Water-*P*	PLT17	Pure water	3.9	2.5	850	189		
	PLT05		11.3	5.0				
	PLT02A[g]		13.0	10			✓	✓
	PLT08		9.3	20			✓	✓
	PLT12		8.9	40			✓	
	PLT31		27.4	80				
Water-*T*	PLT18	Pure water	4.8	10	750	189		
	PLT03		12.9		800			
	PLT02A[g]		13.0		850		✓	✓
	PLT04		13.6		900		✓	
	PLT13		8.0		950			
Water-*t*	PLT15	Pure water	3.4	10	850	6		
	PLT11		4.0			12		
	PLT06		15.7			24	✓	
	PLT07		9.5			48	✓	
	PLT01		7.0			96	✓	✓
	PLT02A[g]		13.0			189	✓	✓
	PLT10A		5.0			384	✓	✓
HCl-*t*	PLT24B	1000 ppm $HCl_{(aq)}$	10.3	10	850	6		
	PLT23B		8.4			12	✓	
	PLT26B		6.7			24	✓	
	PLT30		5.9			48	✓	
	PLT28B		6.8			96	✓	✓
	PLT29B		5.3			189	✓	✓
HF-*t*	PLT24A	1000 ppm $HF_{(aq)}$	7.7	10	850	6		
	PLT25		10.3			12	✓	
	PLT26A		9.0			24	✓	
	PLT27		7.0			48	✓	✓
	PLT28A		4.5			96	✓	✓
	PLT29A		8.1			189	✓	✓

[a]Fluid (pure water, HCl aqueous solution, or HF aqueous solution) enclosed in a gold capsule with the starting material

[b]u_{H2O} gives the mass ratio of water to pumice cubes in the capsule

[c]P indicates the pressure of water impregnated around the vessel as a pressure medium

[d]T refers to the temperature of the sample, measured using a type-K thermocouple attached to the external wall of the vessel

[e]t is the duration for which the pressure and temperature were maintained constant under the target conditions

[f]Check marks indicate the presence of minerals (Crs (> 10 μm): cristobalite larger than 10 μm; Kfs: alkali feldspar) in the sample

[g]PLT02A repeatedly appears as the reference condition for each series of controlled experiments

run charges and starting material (SAK-W) were analyzed on 10–27 rectangular areas of approximately 100 μm^2 for each sample. These regions were devoid of microlites but contained submicron-sized crystals known as nanolites and ultrananolites (Mujin et al. 2017). The standards used for ZAF correction on quantitative values for both minerals and

glasses included GaP (P), wollastonite (Si and Ca), corundum (Al), periclase (Mg), albite (Na), orthoclase (K), and elemental metals (Ti, Fe, and Mn). Elemental mapping was also conducted on selected areas of samples. SEM–EDS (JEOL JCM-7000) was used for elemental mapping. Micro-Raman spectroscopy (JASCO NRS-5100) was used to identify the phases of silica minerals and feldspar in the products. The samples were irradiated using a green excitation laser beam at 532 nm with a power of 7 mW at the source. Each Raman spectrum was acquired in 40 s. The grating of the spectrometer was 1800 lines/mm.

Rhyolite-MELTS calculation

To estimate the remaining fraction of melt at equilibrium and the ideal solidus under experimental conditions, we used the Rhyolite-MELTS program (Gualda et al. 2012) with the glass chemical composition of the starting material SAK-W (Table 1) input as the initial composition. We assumed the oxygen fugacity was set to be NNO ± 0 and simulated water-saturated conditions by adding 20 wt.% H_2O to the system. We confirmed that the calculated mass fraction of the crystallized phases was independent of H_2O content beyond 10 wt.%. Therefore, the chosen amount of H_2O (20 wt.%) did not significantly affect the results.

Results

Groundmass texture and microlite phases

There were no significant changes in groundmass texture and microlite phases among the experimental products using SAK-W and SAK-E as starting materials. This means that the effects of pre-existing microlites on nucleation are not significant as long as glass constitutes the majority of the groundmass. We will focus only on the SAK-W sample hereafter.

Typical groundmass textures formed through the hydrothermal experiments (Run# PLT02A; 850 °C, 10 MPa, and 189 h) are shown in the backscatter electron (BSE) image (Fig. 2a and d) and the same area's combined elemental map with characteristic X-rays of Si Kα, Al Kα, and Mg Kα lines (Fig. 2b and e) and Na Kα, Ca Kα, and K Kα lines (Fig. 2c and f) were assigned to RGB color channels. In Fig. 2b and e, the green, purple, and red regions correspond to feldspars, pyroxene (Px), and silica minerals, respectively. In Fig. 2c and f, yellow to green and blue to purple regions correspond to plagioclase (Pl) and alkali feldspar (Kfs), respectively. the glass-free pores, characteristic of the diktytaxitic texture, were formed in the microlite interstices. At the same time, the quenched glass sporadically remained in the microlite interstices, exhibiting an intersertal texture (orange region in Fig. 2b). Below, we describe the characteristics of microlites crystallized during the experiments.

Feldspars

Feldspar microlites in the sample cross sections were classified into four types according to their size and shape: Type I, large (up to 100 µm in length) and blocky crystals with relatively small aspect ratios; Type II, microlites (approximately 1–50 µm in length) and tabular (elongated on the cross section) crystals; Type III, small (up to 10 µm in length) crystals with thin-platy (elongated on the cross section) and sometimes skeletal shapes; Type IV, the smallest (up to 5 µm in length), thin-platy (elongated on the cross section) crystals. Types I and II are present in both intersertal and diktytaxitic textures. Type-III microlites are found only in the diktytaxitic part, whereas Type-IV microlites were found only in the intersertal part. Type-III crystals were surrounded predominantly by pores, whereas Type-IV crystals were mostly in contact with the glass. Figure 2(c and f) shows that Type-III feldspar is K-rich compared to feldspars of Types I and II, whereas Type-IV feldspar is Na- and Ca-rich. Type-IV feldspar is difficult to distinguish in BSE images and is discernible only in high-resolution, low-noise compositional maps. The minor plagioclase microlites originally contained in SAK-W mainly constitute Types I and II. Types III and IV were not included in the starting materials. Thus, the dominant part of Type-II and all of Type-III and -IV feldspars should have crystallized during the heating experiments.

Figure 3 shows the chemical compositions of Type-II feldspar in the intersertal texture and Type-III feldspar in the diktytaxitic texture of the PLT02A and PLT02B run products, which were run at the reference conditions, i.e., 10 MPa and 850 °C for 189 h. Type-II microlites have plagioclase compositions with $An_{25–45}$ ($An = 100 \times Ca/(Ca + Na + K)$ in mol%). As most Type-III crystals have widths (thickness) of < 1 µm, relatively large (a few µm in width) crystals were selected and measured. Nevertheless, the X-ray excitation area (a few µm in diameter with a 15 keV electron acceleration voltage) could have included the adjacent phases. Hence, the surrounding phases, such as residual glass and Type-II plagioclase, could affect some plots in the miscibility gap. The raw analytical values of Type-III feldspars have K-rich compositions plotted in the miscibility gap at 10 MPa and 850 °C calculated using SOLVCALC (Wen and Nekvasil 1994) based on the thermodynamic model of Nekvasil and Burnham (1987). Data was best interpreted as consisting of two trends: one parallel to the solvus and the other linearly lying between $Ab_{43}Or_{57}$ and the average composition of the residual glass of PLT02A and PLT02B (cross in Fig. 3). The latter linear trend extended to the most Na-rich Type-II plagioclase

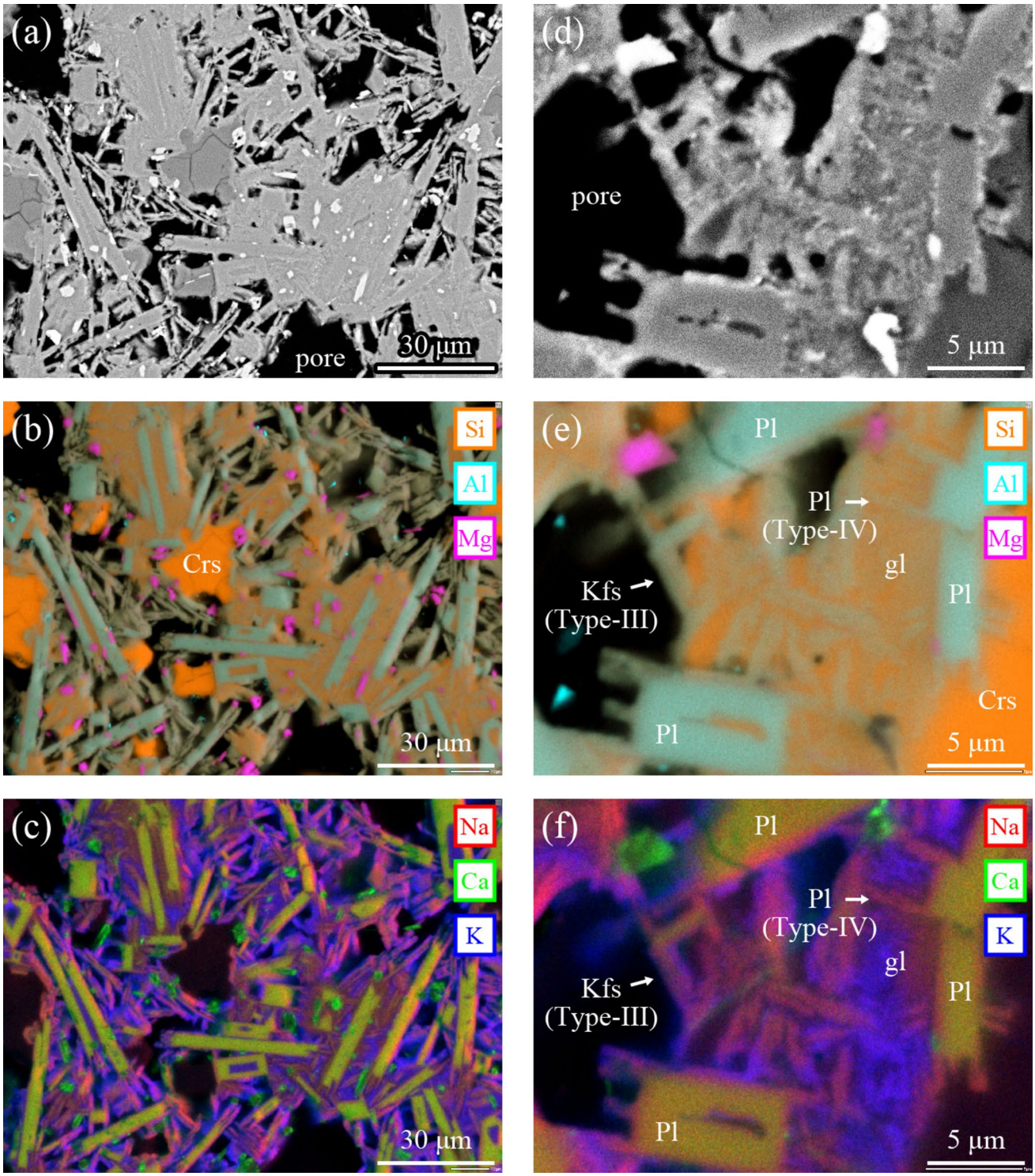

Fig. 2 Typical groundmass textures formed through Run# PLT02A (10 MPa, 850 °C, 189 h, SAK-W). **a**–**c** and **d**–**f** are respectively from the same cross-sectional area. **a**, **d** Backscattered electron images accentuating diktytaxitic pores. **b**, **e** Combined X-ray elemental maps of Si (orange), Al (cyan), and Mg (magenta). The orange, cyan, magenta, and black areas in the maps represent cristobalite, feldspars, pyroxene, and resin-filled pores, respectively, and the remaining light orange areas represent residual glass (gl). **c**, **f** Combined X-ray elemental maps of Na (red), Ca (green), and K (blue). The blue to purple, K-rich thin feldspar microlites compose the diktytaxitic texture (Type-III feldspar). The red to yellow, more Na- and Ca-rich finer feldspar microlites present in the residual glass (Type-IV feldspar). The most Ca-rich fine crystals, corresponding to the Mg-rich ones in **b** and **e**, are pyroxene

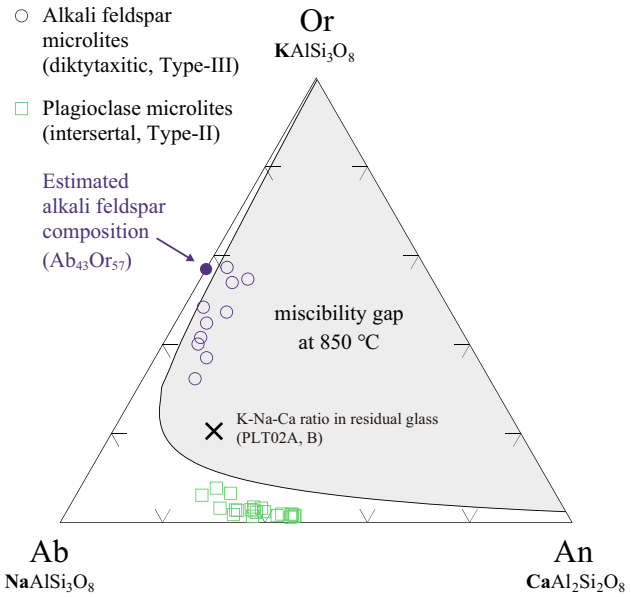

Fig. 3 Or-Ab-An ternary diagram of feldspar microlites crystallized during the experiments of PLT02A (10 MPa, 850 °C, 189 h). Purple open circles and green open squares indicate the compositions of feldspar microlites (Type-III) in the diktytaxitic part and feldspar microlites (Type-II) in the intersertal part, respectively. The gray area is the miscibility gap at 850 °C and 10 MPa, calculated using the software SOLVCALC (Wen and Nekvasil 1994) based on the thermodynamic model of Nekvasil and Burnham (1987). The purple solid circle indicates the estimated composition of alkali feldspar microlites ($Ab_{43}Or_{57}$). The cross shows the average composition of the residual glass of PLT02A and PLT02B

composition. These trends suggest incomplete separation into equilibrium solvus compositions due to rapid crystallization and possible analytical contamination by residual glass and Type-II plagioclase.

Silica minerals

Silica minerals were formed in the interstices of feldspar crystals with a diktytaxitic texture (Fig. 2a and b). This was not observed in the intersertal part; that is, it was not entirely surrounded by residual glass. Raman spectra of the groundmass of the run product at 10 MPa and 900 °C for 189 h (PLT04) showed two sharp peaks at 228 and 417 cm^{-1}, indicating that the silica mineral was cristobalite (Fig. 4a). The cristobalite crystals had characteristic cracks due to the shrinkage upon phase transition from cubic β to tetragonal α at 170–270 °C during quenching (Carpenter et al. 1998; Fig. 2a), as is common for cristobalite in natural volcanic rocks (Baxter et al. 1999; Horwell et al. 2013; Damby et al. 2014). The cristobalite contained up to 2.0 wt.% Al_2O_3 and up to 0.9 wt.% Na_2O (see Supplementary Material, Fig. S1).

Pyroxene

The run products contained fine pyroxene microlites (< 5 µm in length), which should have crystallized during the experiments because they were absent in the starting material. They exhibited both intersertal and diktytaxitic textures. No significant differences in the morphology or size were observed depending on the crystal location.

Fe–Ti oxides

Trace quantities of Fe–Ti oxide microlites were present in the reaction products. They are not discernible in the compositional maps but can be seen in the BSE images (Fig. 2a and d). Most of the Fe–Ti oxide microlites crystallized during the experiments.

In some experiments, euhedral mineral deposits formed small islands on the inner wall of the capsule, away from the pumice sample (Fig. 5a and b). They were of two types: the polyhedron crystals with rounded edges or pyramidal shape up to 20 µm, and aggregates of finer (1–5 µm in diameter) tabular crystals (Fig. 5c and d; PLT04, 10 MPa, 900 °C, and 189 h). In addition to the crystal habits, EDS and Raman analyses showed that the former was cristobalite, whereas the latter was alkali feldspar (Fig. 4b). The exact phase of the alkali feldspar could not be identified, but the doublet Raman peak observed in the range of 450–520 cm^{-1} suggests the alkali feldspar with high degree of Si–Al disorder, namely sanidine (Fig. 4b) (Freeman et al. 2008). Fine acicular crystals were present in the aggregates. The mineral phase of the acicular crystals was not determined owing to their small size, but their morphology and bright BSE contrast suggest that they may be pseudobrookite. Similar island-shaped cristobalite deposits were observed on the sample surfaces (Fig. 5e).

Textural evolution at 850 °C and 10 MPa in halogen-free and halogen-bearing systems

The composition maps of the Water-*t* series run products, a pure water-saturated time study with SAK-W as the starting material, showed that the interstitial residual glass decreased with increasing run duration (Fig. 6a–f). The number density of mappable plagioclase microlites (Type-II feldspar) increased with time. A small quantity of cristobalite appeared in 6–12 h, and large (> 10 µm) cristobalite crystals appeared after 24 h. The typical diktytaxitic pores, which have a polygonal shape surrounded by crystal faces, became apparent at 96–189 h as the Type-III alkali feldspar formation progressed. After 189 h, the quantity of interstitial residual glass was negligible and the groundmass became

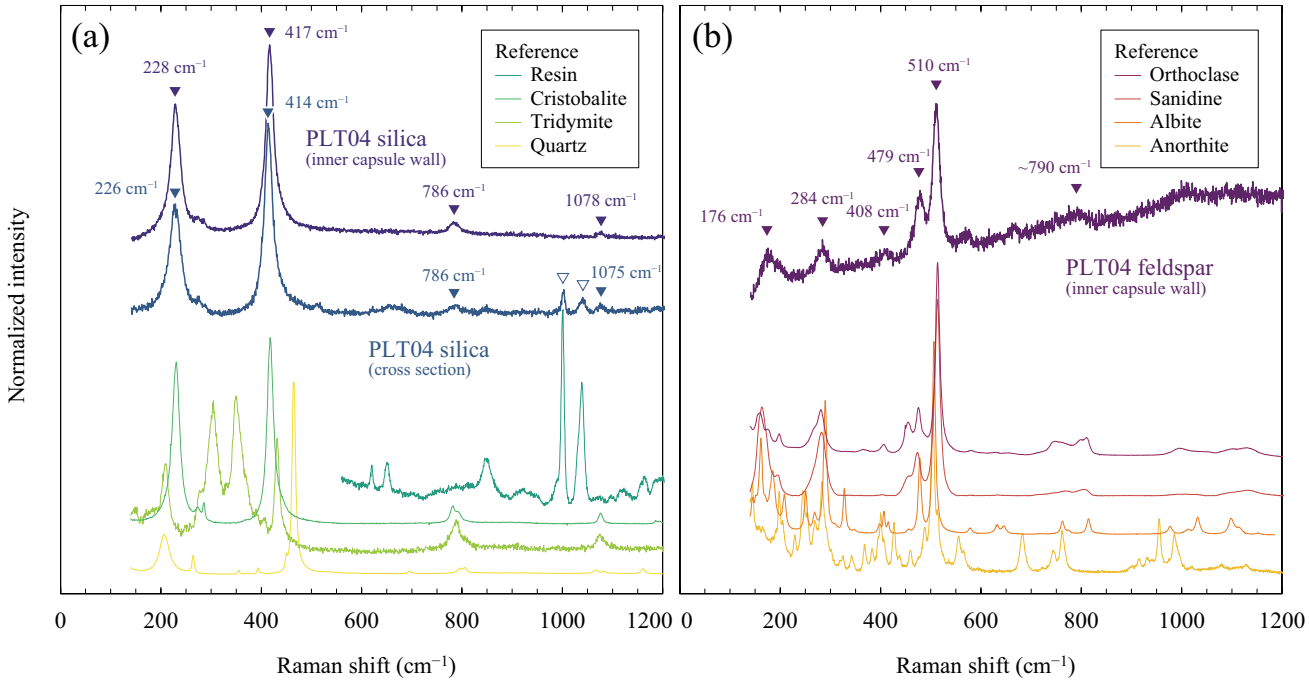

Fig. 4 Representative Raman spectra of silica minerals and feldspar microlites crystallized in Run# PLT04 (10 MPa, 900 °C, 189 h). **a** Silica minerals deposited on the inner capsule wall and found in the cross-section of the run product. The reference spectra of the resin, cristobalite (Kingma and Hemley 1994), tridymite (Kingma and Hemley 1994), and quartz (Gillet et al. 1990) are also shown. **b** Feldspar microlites deposited on the inner capsule wall. Reference spectra of orthoclase (Fabel et al. 1972), sanidine (R06013 from RRUFF database, Lafuente et al. 2015), albite (Fabel et al. 1972), anorthite (Daniel et al. 1995) are also shown. All spectral intensities are normalized to their maximum values

dominantly diktytaxitic. The rounded vesicle outlines remained until 96 h, whereas the interstitial pores with a diktytaxitic texture predominated at 189 h.

In the HCl- and HF-bearing systems, the textural evolution was similar to that observed in the halogen-free experiments (Fig. 6g–l, m–r). However, cristobalite crystals larger than 10 µm appeared in both series in 12 h, half the time for the Water-*t* series. Type-III alkali feldspar became conspicuous after 96 h for all gas compositions. The thin and tabular, fine-grained (< 8 µm in diameter) alkali feldspar aggregates were observed on the inner capsule wall in the 48-h experiment (PLT27) of the HF-*t* series (Fig. 5f).

Dependence on water–rock ratio

The experimental products controlling the water–rock ratio (Water-*u* series) did not show systematic differences in mineral assemblages, crystal sizes, proportion of intersertal to diktytaxitic areas (i.e., ratios of residual glass and Type-III alkali feldspar microlites), and modal proportion and number density of cristobalites (Fig. 7). On the other hand, the porosity increased with increasing water proportion, probably because the free fluid in the Au capsule mitigated pumice compaction during the initial pressurization of the hydrothermal experiments.

Pressure dependence

Results of the control experiments on pressure (Water-*P* series; Fig. 8a–e) showed that the pumice groundmass transformed to a diktytaxitic texture almost entirely within the experimental duration (189 h) at 10 and 20 MPa. The size of cristobalite crystals increased with pressure, reaching ~30 µm at 20 MPa. These changes were significant between 5 and 10 MPa.

The modal proportion of Type-II plagioclase microlites was maximized at 10–20 MPa. In other words, the microlite interstices decreased with increasing pressure from 2.5 to 10–20 MPa, and then, increased to 40 MPa. BSE images revealed that abundant nanolites that are not resolved in the compositional maps existed in the microlite interstices (Fig. 9a–e). The heterogeneous nucleation of acicular nanolites on Type-I and Type-II plagioclase surfaces was conspicuous at 10–20 MPa. The microlite interstices are mostly filled with nanolites at a pressure of ≤ 10 MPa, while glass is barely discernible at 20 MPa and dominant at 40 MPa, indicating that the fluid-saturated solidus lies between 10 and 20 MPa at 850 °C.

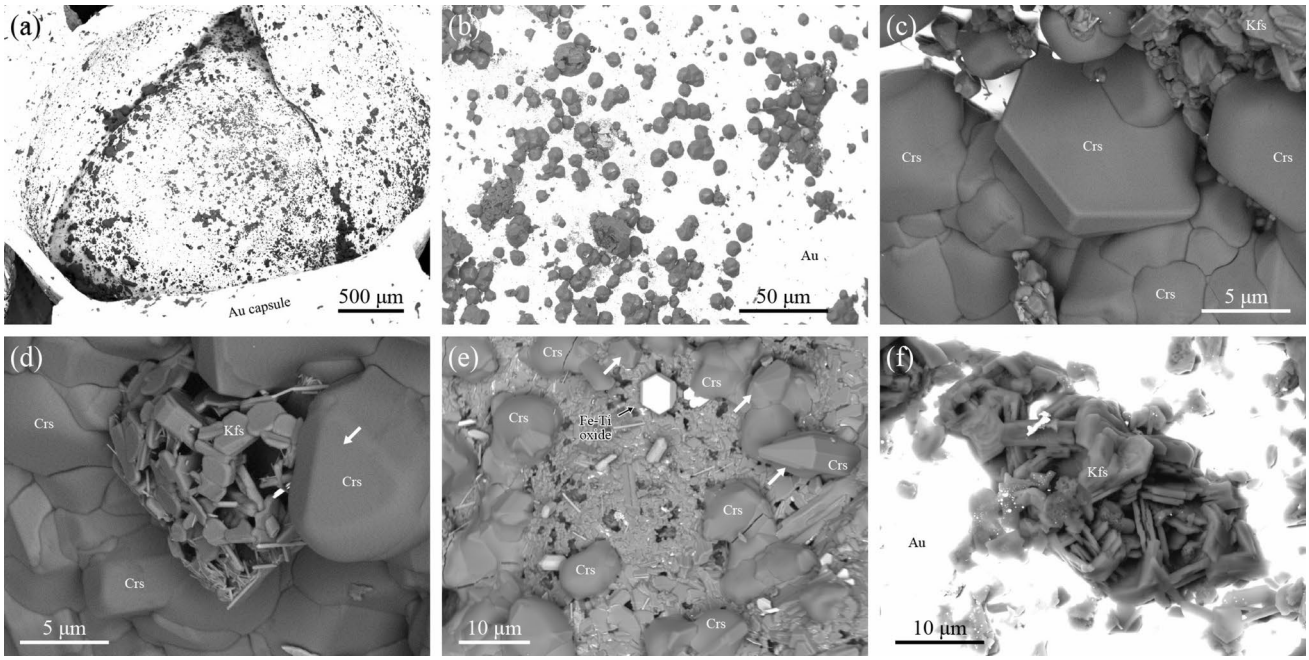

Fig. 5 Backscattered electron images of crystals deposited on the internal walls of capsules and pumice samples. **a**, **b** Euhedral mineral deposits occurred as small islands on the inner Au capsule wall of Run# PLT07 (10 MPa, 850 °C, 48 h). **c**, **d** Blocky cristobalite crystals (Crs) with sizes up to 20 µm and aggregates of tabular alkali feldspar microlites (Kfs) deposited on the inner Au capsule wall of Run# PLT04 (10 MPa, 900 °C, 189 h). **e** Island-shaped cristobalite (Crs) crystals and a euhedral Fe–Ti oxide crystal on the pumice sample in Run# PLT02B (10 MPa, 850 °C, 189 h). **f** Aggregates of skeletal microlites (Kfs) deposited on the inner Au capsule wall of Run# PLT27 (10 MPa, 850 °C, 48 h with $HF_{(aq)}$)

Temperature dependence

Control experiments at a temperature of 10 MPa (Water-*T* series) showed that the diktytaxitic area fraction and modal proportion of cristobalite increased with increasing temperature from 750 to 850 °C (Fig. 8f–j). At 900 °C, the area of diktytaxitic texture was limited to the periphery of vesicles, and most of the groundmass showed intersertal texture with residual glass. At 950 °C, the groundmass showed intersertal texture with rounded vesicles and no diktytaxitic textures formed. The run products at 750 and 800 °C showed similar groundmass textures to those at 2.5 and 5.0 MPa and 850 °C, with minor diktytaxitic portions and relatively fine-grained cristobalite.

Abundant nanolites were formed in the microlite interstices at ≤ 900 °C (Fig. 9f–j). The size of the nanolites decreased with decreasing temperature (Fig. 9f–j). The residual glass became clear at 900 °C, indicating that the solidus existed between 850 and 900 °C at 10 MPa. Heterogeneous nucleation of acicular nanolites on the plagioclase microlites was observed at 800–900 °C.

Temporal changes in chemical compositions of each phase

In Fig. 10a, we provide an overview of the temporal changes in the chemical compositions of each phase in the run products of SAK-W from the Water-*t* series, that is, Type-II plagioclase, Type-III alkali feldspar, cristobalite, pyroxene, and glass, in terms of K_2O versus Al_2O_3 concentration. We note that nanolites, ultrananolites, and Type-IV Na-rich plagioclase, if present, are included in the glass analyses because of the limitation of spatial resolution. Among the major elements in the experimental system, Al_2O_3 was more refractory than SiO_2, whereas K_2O behaved as an incompatible element before the crystallization of K-rich feldspar, representing the differentiation process of the residual melt. As shown in Fig. 3, the K_2O content of alkali feldspar (Type IV) varied widely from 5.7 to 9.6 wt.%, which corresponds to Or# (= K/(Na + K + Ca) in mol%) 32–57. The alkali feldspar compositions were analyzed only for the 189-h run (PLT02A and PLT02B) because the crystal size did not reach the minimum analyzable size in the shorter runs. Nevertheless,

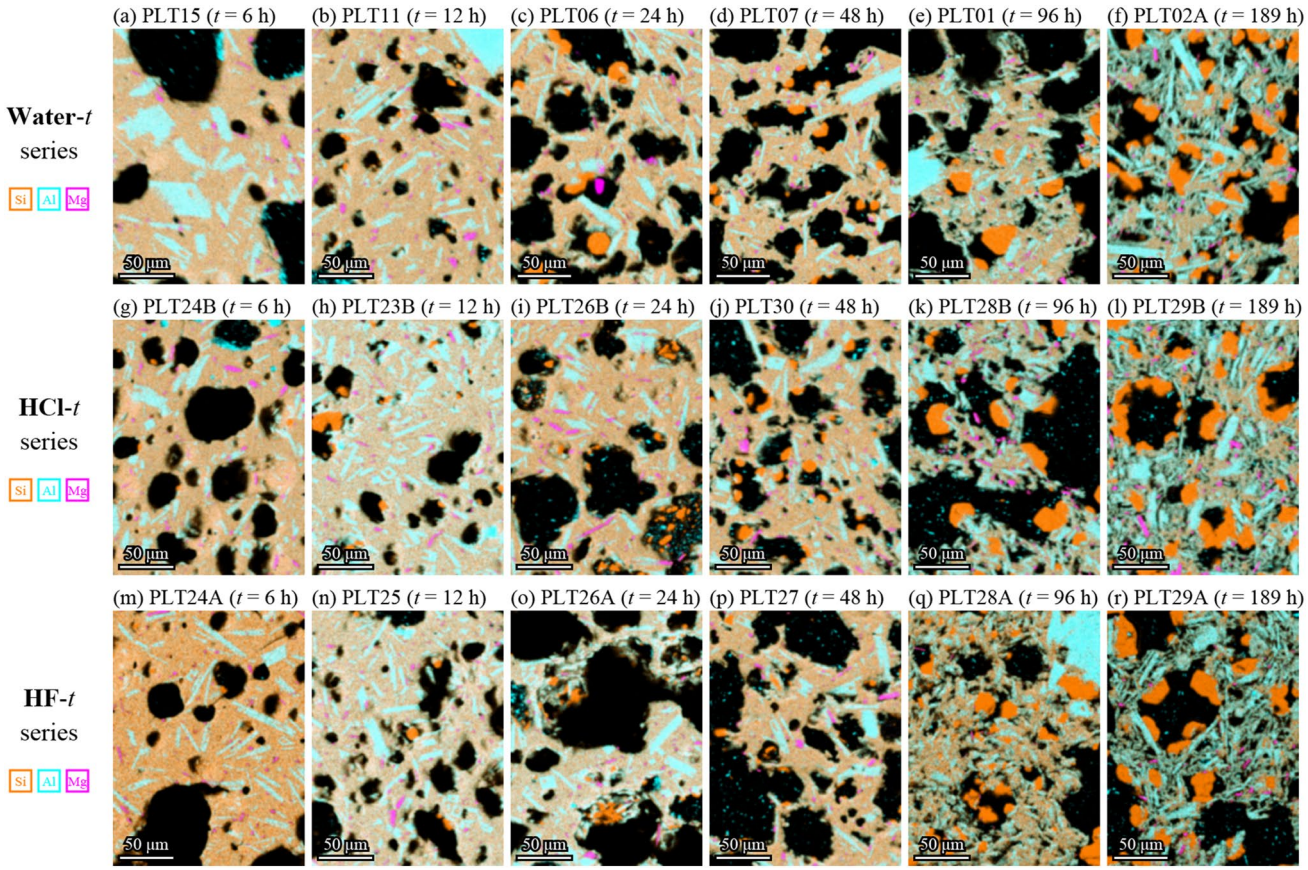

Fig. 6 Combined X-ray elemental maps of Si (orange), Al (cyan), and Mg (magenta) of cross-sections of the run products from the experimental series of Water-*t* (**a–f**), HCl-*t* (**g–l**), and HF-*t* (**m–r**). The orange, cyan, magenta, and black areas in the maps represent cristobalite, feldspars, pyroxene, and resin-filled pores, respectively, and the remaining light orange areas represent residual glass

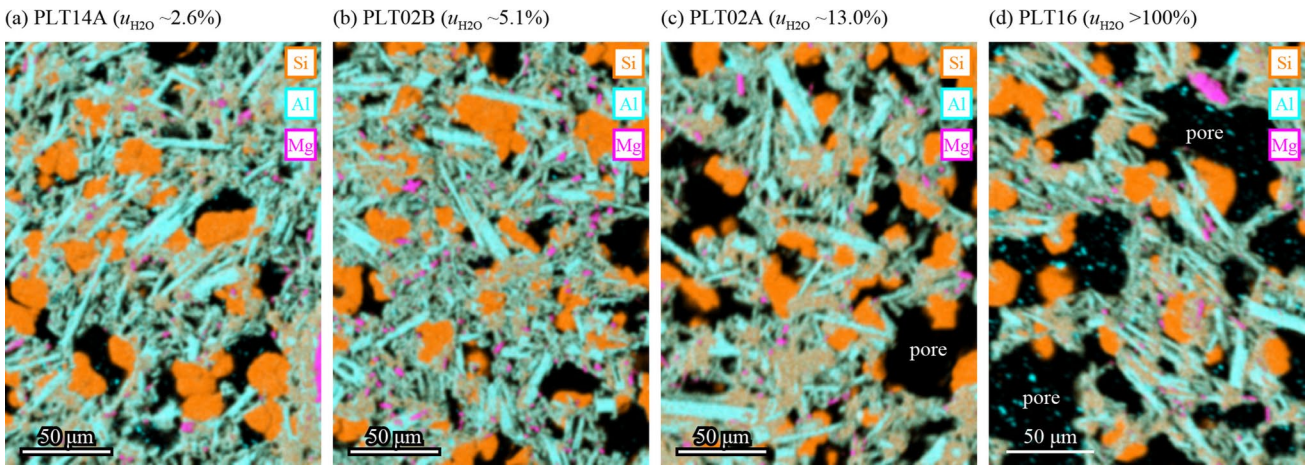

Fig. 7 Combined X-ray elemental maps of Si (orange), Al (cyan), and Mg (magenta) of cross-sections of the experiments with different water–rock ratios (2.6–13% and > 100%) from the Water-*u* series. The orange, cyan, magenta, and black areas in the maps represent cristobalite, feldspars, pyroxene, and resin-filled pores, respectively, and the remaining light orange areas represent residual glass

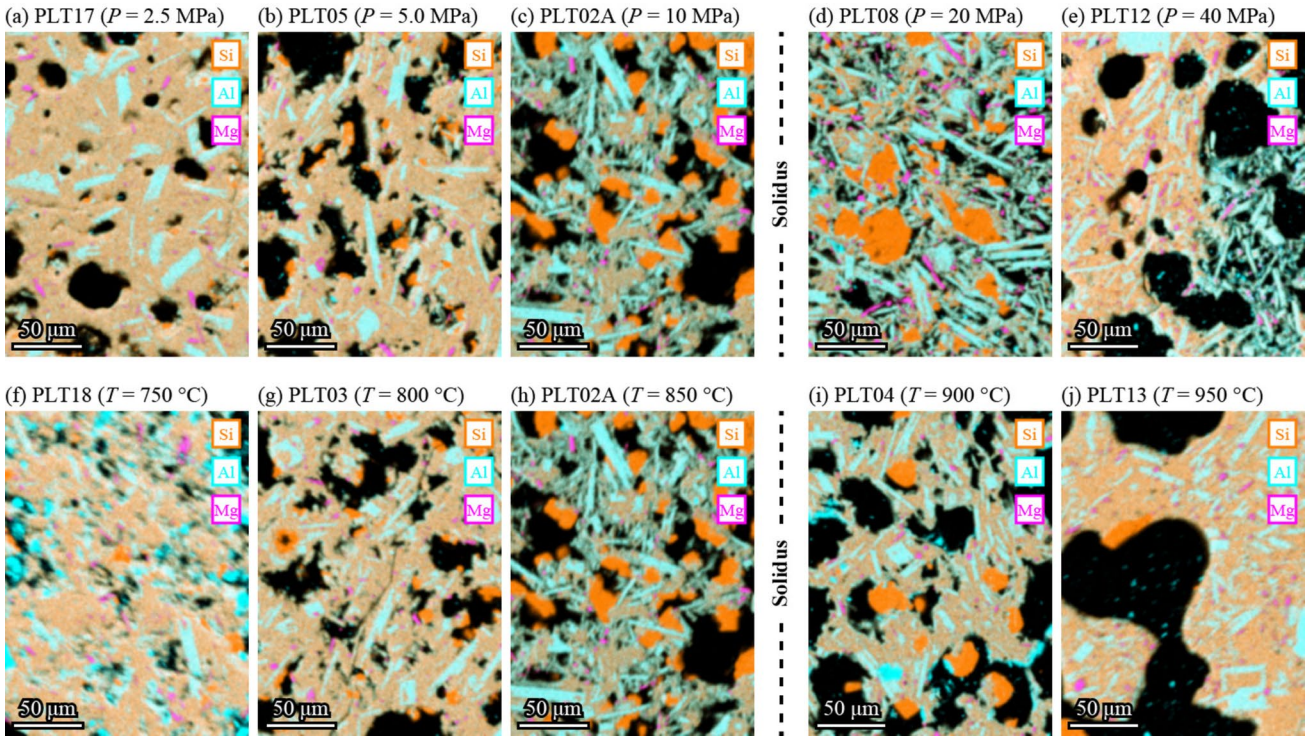

Fig. 8 Combined X-ray elemental maps of Si (orange), Al (cyan), and Mg (magenta) of cross-sections of the samples heated at different pressures (2.5–40 MPa) and a fixed temperature (850 °C) from the Water-*P* series (**a**–**e**), and at different temperatures (750–950 °C) and a fixed pressure (10 MPa) from the Water-*T* series (**f**–**j**). The orange, cyan, magenta, and black areas in the maps represent cristobalite, feldspars, pyroxene, and resin-filled pores, respectively, and the remaining light orange areas represent residual glass. The dashed lines separate sub- and supra-solidus conditions calculated using Rhyolite-MELTS (see Fig. 12)

Type-III alkali feldspar crystals show compositional zoning from Na- to K-rich from the core to the rim (Fig. 2c and f), indicating that their compositions became more K-rich with time. The composition of alkali feldspar ($Ab_{43}Or_{57}$) estimated from Fig. 3 is shown in Fig. 10a.

The K_2O concentrations of the glasses showed a systematic evolution with run duration. Until 48 h, K_2O increased from 2.84 to 5 wt.%, while Al_2O_3 was almost constant at 11–12%. After reaching the tie-line of cristobalite and $Ab_{43}Or_{57}$, K_2O started to decrease until ~ 1 wt.%, passing the initial glass composition with a slight Al_2O_3 increase to ~ 15 wt.%. The Type-II plagioclase compositions also showed a variation with the experimental duration; the An content decreased from 44–52 to 25–39 mol%, and K_2O increased from 0.15–0.38 to 0.23–1.24 wt.% (Fig. 10a), approaching the solvus shown in Fig. 3. In cristobalite, Al_2O_3 and K_2O were contained up to 2 and 0.06 wt.%, respectively.

The temporal variation in the K_2O concentration in the glass is highlighted in Fig. 10b–d for different vapor compositions. In the halogen-free system (Water-*t* series), the glass K_2O concentration began to increase at 6 h after the onset of the experiments, reached a maximum at 48 h, and then decreased. The K_2O concentration decreased to values lower than those of the starting composition after approximately 100 h. In the halogen-bearing systems (HCl-*t* and HF-*t* series), the K_2O concentrations exhibited a temporal evolution similar to that of the halogen-free system (Water-*t* series). It could have started to increase slightly faster in the halogen-containing systems, but the error bars show that the difference was not significant (Fig. 10c and d).

Discussion

In this study, the conditions required for the formation of a diktytaxitic texture were systematically examined. In all the experimental series of Water-*t*, HCl-*t*, and HF-*t*, cristobalite started to crystallize within the shortest experimental duration (6 h). This is consistent with the fact that cristobalite or tridymite accompanies natural volcanic rocks with diktytaxitic textures, such as dome lavas, blocks and ash flows derived from domes, and volcanic ash plumes through open conduits (Schipper et al. 2015, 2017; Kushnir et al. 2016). Furthermore, alkali feldspar was found to crystallize in the later stages of the formation of the

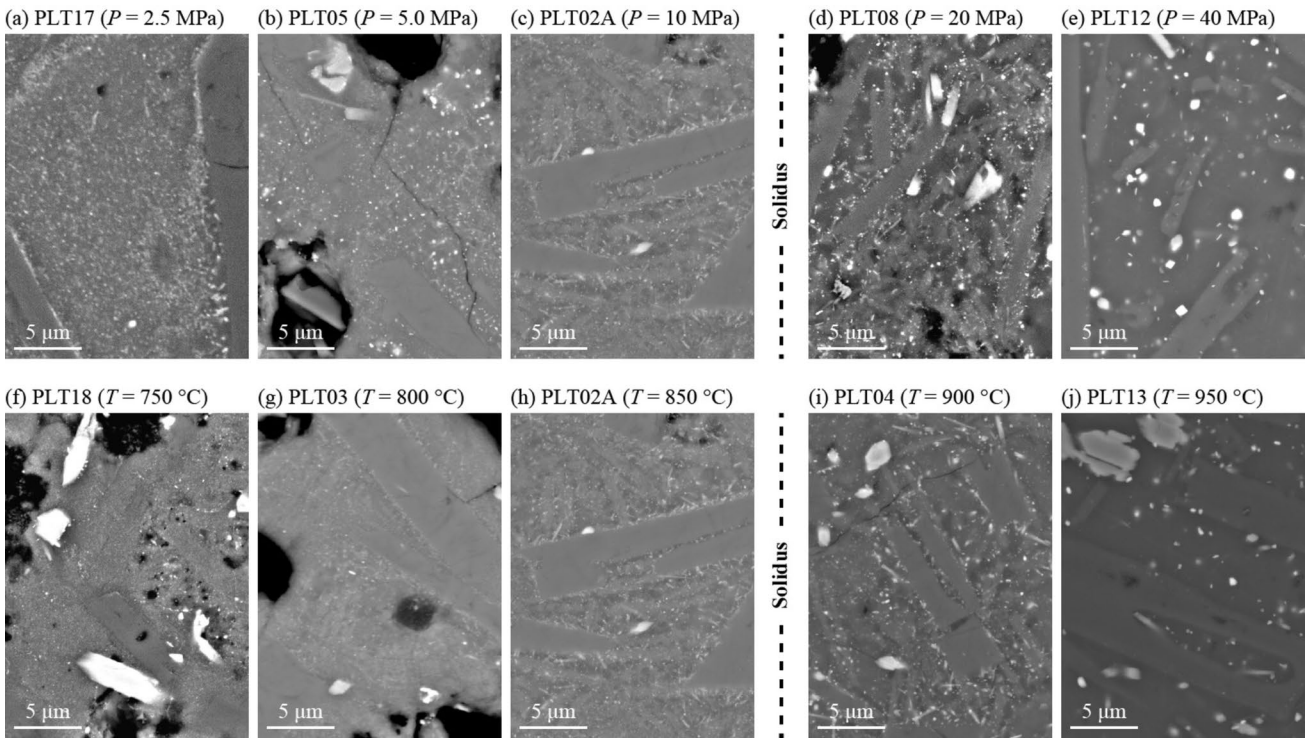

Fig. 9 Backscattered electron images of the residual glass of the samples heated at different pressures (2.5–40 MPa) and a fixed temperature (850 °C) from the Water-*P* series (**a**–**e**), and at different temperatures (750–950 °C) and a fixed pressure (10 MPa) from the Water-*T* series (**f**–**j**). The tiny bright crystals are mafic nanolites. The dashed lines separate sub- and supra-solidus conditions calculated using Rhyolite-MELTS (see Fig. 12)

diktytaxitic texture. Thus, we first discuss the crystallization processes of cristobalite and alkali feldspar.

Deposition of cristobalite and alkali feldspar

Cristobalite in volcanic rocks has been interpreted as either (1) vapor-phase (pneumatolytic) deposition or (2) crystallized from glass ("devitrification") (e.g., Horwell et al. 2013). The deposition of cristobalite on the inner wall of the capsule, which was not in contact with the starting material during the experiment, was direct evidence of deposition from the vapor. The prismatic shape of cristobalite is consistent with the characteristics of vapor-phase cristobalite deposits reported in natural volcaniclastic rocks (e.g., Horwell et al. 2013). In addition, the absence of a residual glass covering the cristobalite supports the origin of its vapor phase. In contrast, no silica minerals directly crystallized from the supercooled melt were observed in this study. Horwell et al. (2013) identified patchy silica minerals intergrown with feldspar microlites in lava dome rocks as cristobalite using micro-Raman spectroscopy, and concluded that cristobalite was formed through devitrification. No patchy structures or other intergrowths were observed in our run products. Therefore, we conclude that all cristobalite crystals in the present experiments were formed via deposition from the vapor phase.

Under all experimental conditions used in this study, cristobalite was in a metastable phase. The stable phase of pure SiO_2 is β-quartz (< 870 °C) or tridymite (> 870 °C), while cristobalite is stable at a much higher temperature (> 1470 °C; Deer et al. 2013). It is known that the Al^{3+} and Na^+ couple substitute Si (Chao and Lu 2002). In addition, the presence of alkaline ions (Dapiaggi et al. 2015) and alumina (Liang et al. 2017) enhances the metastable retention of cristobalite. The cristobalite crystals produced in this study contained Al_2O_3 (up to 2.0 wt.%) and Na_2O (up to 0.9 wt.%). In β-cristobalite, which is considered to be the first deposited phase of silica in this experiment, the crystal structure might be stabilized due to the substitution of Si^{4+} by Al^{3+} or the Na^+ and Al^{3+} interstitial ions (Chao and Lu 2002). Our experimental results are also consistent with those of Martel et al. (2021), in which cristobalite coexisted with melts having a wide range of SiO_2 contents (70–81 wt.%) at pressures below 20–30 MPa and temperatures from sub-solidus to near liquidus.

The deposition of alkali feldspar on the inner capsule walls is the direct evidence of its occurrence in the vapor phase. These crystals typically have thin tabular shapes (Fig. 5d and f). The 2D cross-section revealed that some

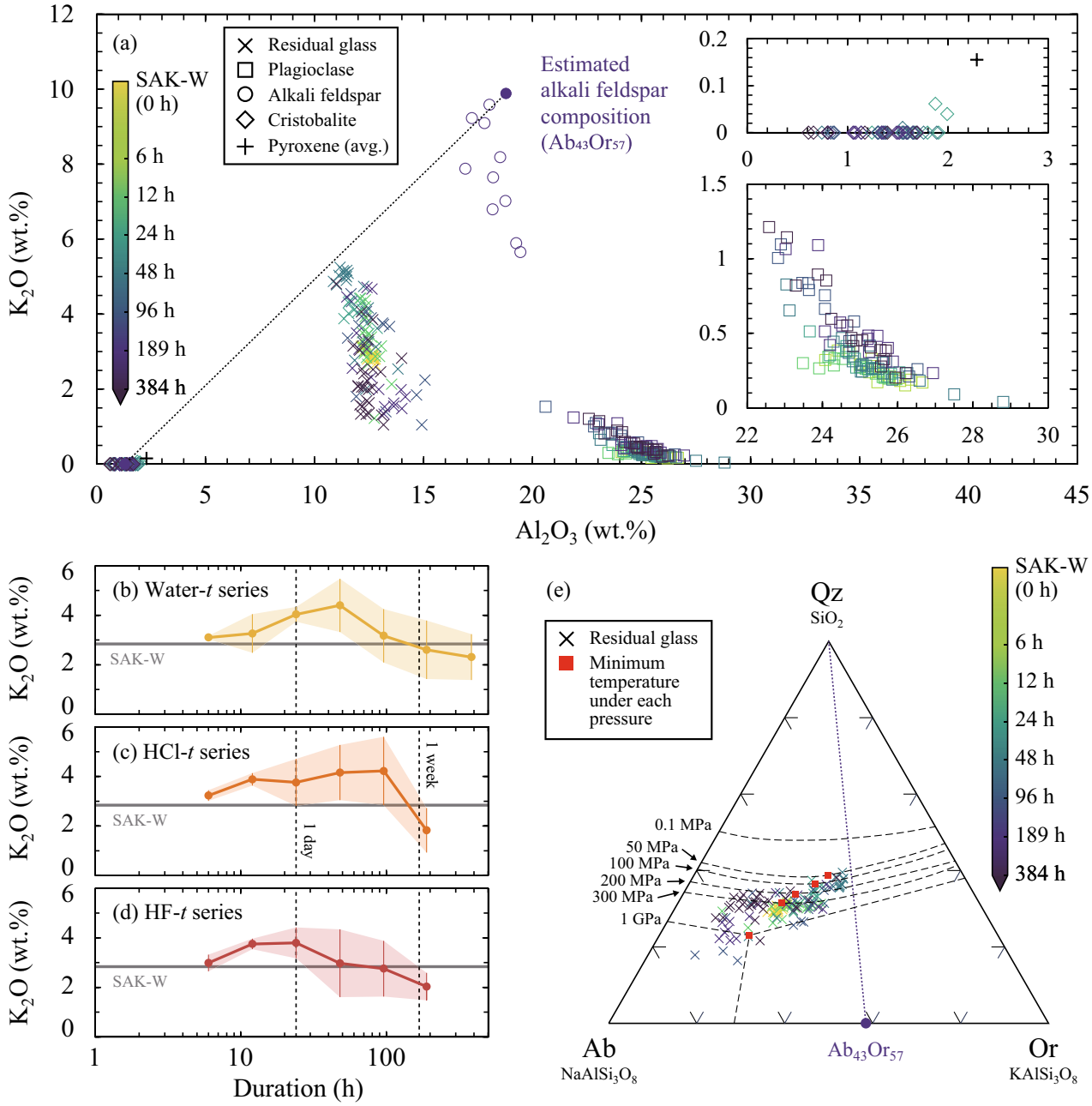

Fig. 10 **a** Al_2O_3 versus K_2O diagram of the residual glass (cross), Type-II plagioclase microlites (open squares), Type-III K-rich feldspar microlites (open circles), cristobalite (diamonds), and average pyroxene (plus) from Water-*t* series. Symbol colors indicate heating durations as shown in the color bar. The dotted line connects the average composition of cristobalite crystals and the assumptive composition of alkali feldspar microlites ($Ab_{43}Or_{57}$, solid circle). The cristobalite and plagioclase compositions are shown enlarged in the insets. **b**–**d** Temporal changes of K_2O concentration of residual glass in the run products from the experimental series of **b** Water-*t*, **c** HCl-*t*, and **d** HF-*t*. Error bars indicate one standard deviation. **e** Residual glass compositions (cross) plotted on a Qz–Ab–Or ternary diagram (in weight) based on the EDS quantitative analyses of SiO_2, Al_2O_3, Na_2O, and K_2O. Symbol colors indicate the heating durations, as shown in the color bar. Cotectic lines (dashed curves) and compositions of H_2O-saturated minima (red squares) are from Blundy and Cashman (2001) and references therein

alkali feldspars formed within the pumice samples (Type III) were thinner and often skeletal (Fig. 2). BSE images and X-ray compositional map showed that Type-III alkali feldspars were mostly found in the pores. Alkali feldspar crystals that were completely covered by the melt were not observed (Fig. 2). These observations show that most, if not all, of the Type-III alkali feldspar microlites crystallized from vapor rather than from the melt. The reason for the difference in

the crystal shape between the alkali feldspar deposited on the capsule walls and that in the pumice pores was not apparent. Because heterogeneous nucleation was assumed for deposition in both cases, the substrate conditions and deposition timing (consequently, the degree of supersaturation for crystal growth) may have been different.

The present experiments demonstrate that the formation of diktytaxitic texture and vapor-phase minerals proceeds under near-solidus conditions in the presence of water vapor in a relatively low-pressure subvolcanic system. Under such conditions, crystal growth in the residual melts must be sluggish because the elemental diffusivity in the melt is low, owing to the low temperature and low dissolved water content. Therefore, we interpret that the crystallization of the system proceeded through a faster process, that is, selective evaporation and deposition of the silica mineral and alkali feldspar components. In contrast to cristobalite and Type-III alkali feldspar, Type-IV albite-rich plagioclase crystals were found mostly in the residual glasses (Fig. 2), indicating that they grew from the supercooled melt enriched in the albite component because of the selective evaporation of silica and alkali feldspar. The reason for this contrasting behavior remains to be determined. However, the activation energy of any elementary process for plagioclase, including evaporation, nucleation, and growth from vapor, can be higher than those of silica minerals and alkali feldspar.

Formation processes of diktytaxitic texture and evolution of melt composition

Time-series experiments showed that interstitial voids of the diktytaxitic texture were formed via the regression of the melt surfaces by evaporation, counteracting the deposition of cristobalite and alkali feldspar in the pores (Fig. 6). The large (> 10 μm) cristobalite deposits appeared in 12–24 h (6–12 h with HF/HCl), alkali feldspar microlites (Type-III) started to deposit in 2–4 days (1–2 days with HF/HCl), and crystallization of small Na-rich feldspar microlites (Type-IV) in melt terminated the formation of diktytaxitic texture within 4–8 days (Fig. 11a–d). The timing of evaporation–deposition can also be estimated from the change in the glass composition. The growth of Type-II plagioclase from the melt and the evaporation of SiO_2 led to the melt composition approaching the tie-line between cristobalite and the alkali feldspar composition ($Ab_{43}Or_{57}$), followed by the evaporation of the alkali feldspar components, resulting in a decrease in K_2O in the melt (Fig. 11c).

The depletion of CaO from the melt at a relatively early stage by Type-II plagioclase growth allowed us to examine the evolution of the melt composition in the Ab–Or–Q ternary system. We plotted the time-resolved melt compositions along with cotectic lines at 0.1–1000 MPa determined experimentally (Blundy and Cashman 2001; Fig. 10e). Notably, because the experiments were conducted under isothermal conditions near the solidus temperature, the temporal change in the melt composition does not represent the liquid line of descent but reflects the kinetics of isothermal crystallization from the supercooled melt. Nevertheless, plotting data on this phase diagram is helpful in understanding the mineral phases that derive the evolution of the melt composition. The tie-line between Qz and $Ab_{43}Or_{57}$ is close to the temperature minimum of the cotectic boundary, supporting the appropriateness of using this phase diagram. The melt compositions plot roughly parallel to the cotectic lines between Qz and the alkali feldspar solid solution. After 48 h, the melt compositions were controlled by the fractionation of Ab (Type-II plagioclase) and Qz (cristobalite) and reached the tie-line between Qz and $Ab_{43}Or_{57}$. After 96 h, the fractionation of Or (alkali feldspar) in addition to Qz drove melt differentiation toward the Ab apex beyond the starting composition. Type-IV Na-rich plagioclase was assumed to have crystallized from this late-stage melt enriched with the albite component.

Vapor-phase silica species

Based on the linear relationship between the partial pressure of H_2O and that of Si species with a slope of ~ 2, Hashimoto (1992) demonstrated that $Si(OH)_{4(g)}$ is the dominant gaseous Si species when solid silica reacts with high-temperature water vapor, which is explained by the following equation:

$$SiO_{2(s)} + 2H_2O_{(g)} \leftrightarrow Si(OH)_{4(g)}. \quad (1)$$

According to thermodynamic calculations, the most abundant gaseous Si species coexisting with water vapor at 850 °C and 5–10 MPa in equilibrium with quartz is $Si(OH)_{4(g)}$, with the partial pressure at more than 10^{10} times higher than that of $SiO_{2(g)}$ and $SiO_{(g)}$ (Plyasunov 2011, 2012). Using mass spectrometry, Opila et al. (1997) showed that $Si(OH)_{4(g)}$ was the main stable gaseous silicon species at 1200–1400 °C in a flowing water vapor–oxygen gas mixture at a total pressure of 1 bar.

The dissolution of silicate glass in water has been extensively studied. It consists of a sequential process of adsorption (and diffusion) of water molecules, ion exchange, and hydrolysis (e.g., Gin et al. 2021 and references therein). The rate-limiting step in this overall reaction is probably either elemental diffusion in the melt or one of the hydrolysis reaction steps of siloxane bonds by water (≡Si–O–Si≡ → ≡Si–OH + HO–Si≡) unless an Si-rich amorphous layer is formed on the glass surface, preventing the diffusive transport of aqueous species (Fig. 11e).

The alkali feldspar deposition found in the present experiments indicates that K and Al are also mediated by water

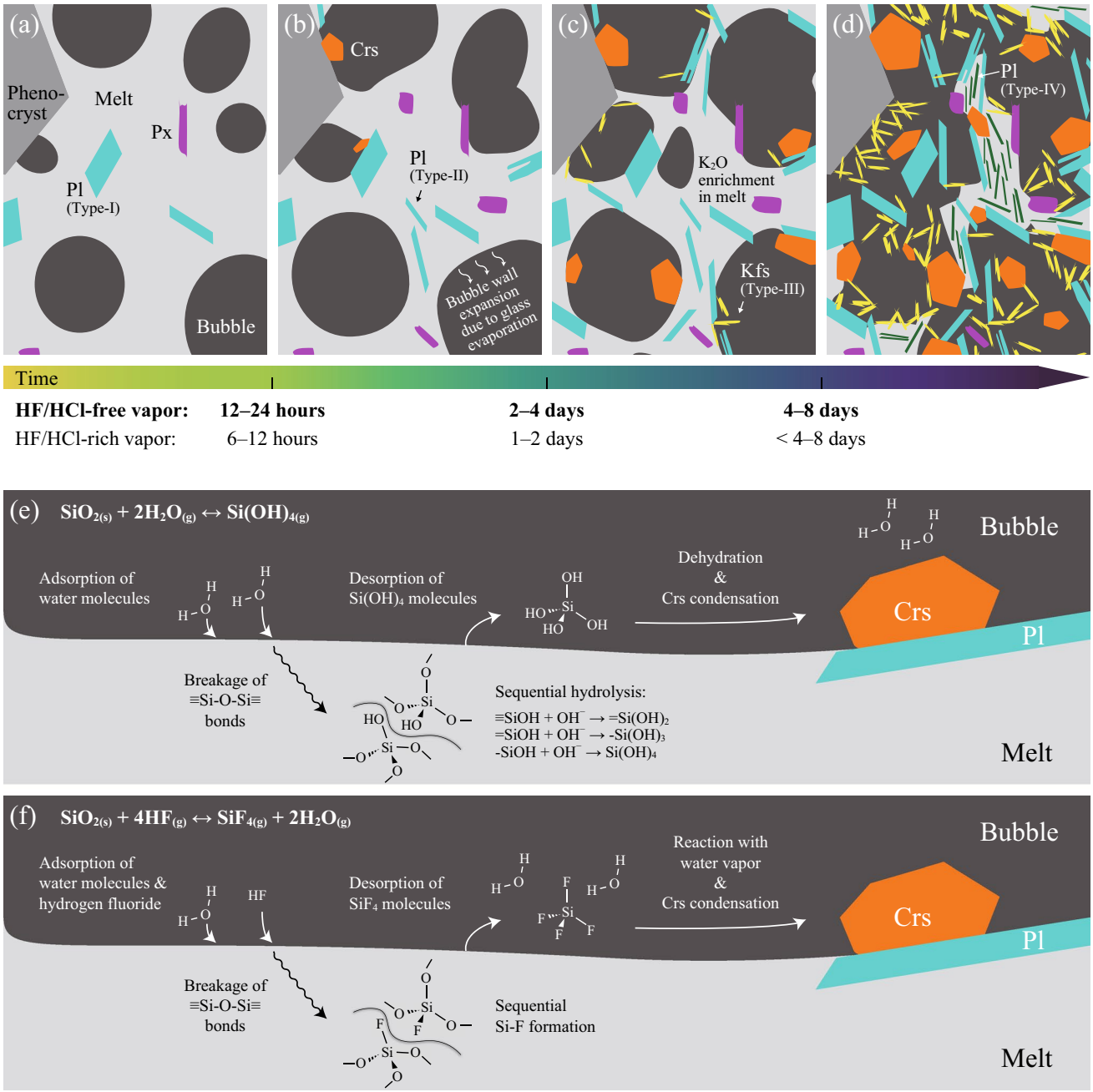

Fig. 11 **a–d** Schematic illustrations of the formation process of diktytaxitic textures. **a** Rhyolitic to andesitic magma in a lava dome or a shallow volcanic conduit initially contains phenocrysts (plagioclase, pyroxene, and Fe–Ti oxide: dark gray), and microlites of Type-I plagioclase (cyan) and pyroxene (magenta) surrounded by near-solidus melt (light gray) and bubbles. **b** 12–24 h (6–12 h in HF/HCl-rich environment) after the magma intrusion, Type-II plagioclase crystallizes, and melt front regression and cristobalite (orange) deposition occur onto the bubble walls or surfaces of crystals exposed to vesicles via evaporation and deposition of melt. **c** 2–4 days (1–2 days in HF/HCl-rich environment) after the magma intrusion, crystallization of cristobalite and feldspar causes enrichment of K_2O in melt followed by onset of vapor-phase deposition of Type-III alkali feldspar microlites (yellow). **d** Within 4–8 days (probably shorter in HF/HCl-rich environment) after the magma intrusion, the formation of diktytaxitic texture is terminated by pervasive melt evaporation, deposition of cristobalite and alkali feldspar, and crystallization of Type-IV small feldspar microlite (dark green) in the melt. **e–f** Schematic summary of the silica evaporation–deposition mechanism from melt to cristobalite in **e** HF/HCl-free and **f** HF-rich systems

vapor. Hashimoto (1992) reported that $Al(OH)_{3(g)}$ is the dominant gaseous Al species coexisting with H_2O. Considering these gaseous species, the overall reaction for alkali feldspar transport can be described as follows:

$$KAlSi_3O_{8(s)} + 8H_2O_{(g)} \leftrightarrow KOH_{(g)} + 3Si(OH)_{4(g)} + Al(OH)_{3(g)}. \quad (2)$$

Effect of halogens

This study demonstrates that diktytaxitic texture and vapor-phase deposits of both cristobalite and alkali feldspar were formed in a halogen-free system. In the previous studies, the diktytaxitic rims around the vesicles have been interpreted as corrosion rinds resulting from corrosion of the groundmass melt or glass by gaseous hydrogen halides such as HF and HCl in volcanic gases and redeposition via gaseous species such as SiF_4 and $SiCl_4$ (De Hoog et al. 2005; Horwell et al. 2013; Schipper et al. 2015, 2017, 2019). These reactions are expressed as follows:

$$SiO_{2(s)} + 4HCl_{(g)} \leftrightarrow SiCl_{4(g)} + 2H_2O_{(g)}, \quad (3)$$

$$SiO_{2(s)} + 4HF_{(g)} \leftrightarrow SiF_{4(g)} + 2H_2O_{(g)}. \quad (4)$$

In the system containing both Cl (HCl-*t* series) and F (HF-*t* series), cristobalite crystals larger than 10 µm appeared in both series in half the time for the Water-*t* series, and the increase of K_2O concentration in the glass proceeded slightly faster compared to the system without halogen (Water-*t* series). This reflects the positive effects of $SiCl_{4(g)}$ and $SiF_{4(g)}$ in addition to $Si(OH)_{4(g)}$ (Fig. 11f). Adding both HCl and HF slightly accelerated the crystallization process but did not show significant effects on the evolution of groundmass texture and glass chemical composition (Figs. 6 and 10b–d).

Conditions of formation of diktytaxitic texture

We calculated the equilibrium mass fractions of constituent phases using the rhyolite-MELTS program (Gualda et al. 2012) for the glass composition of the starting material (SAK-W) at a fixed temperature (850 °C) with varying pressures (Fig. 12a) and at a fixed pressure (10 MPa) at varying temperatures (Fig. 12b). The solidus was determined to be 19 MPa at 850 °C and 870 °C at 10 MPa, showing excellent agreement with the estimation from the Water-*P* and Water-*t* series experiments. The appearance of silica minerals at a relatively high temperature of 10 MPa and the crystallization of alkali feldspar within a narrow temperature range in the pseudo-eutectic solidus were also consistent with the experimental results.

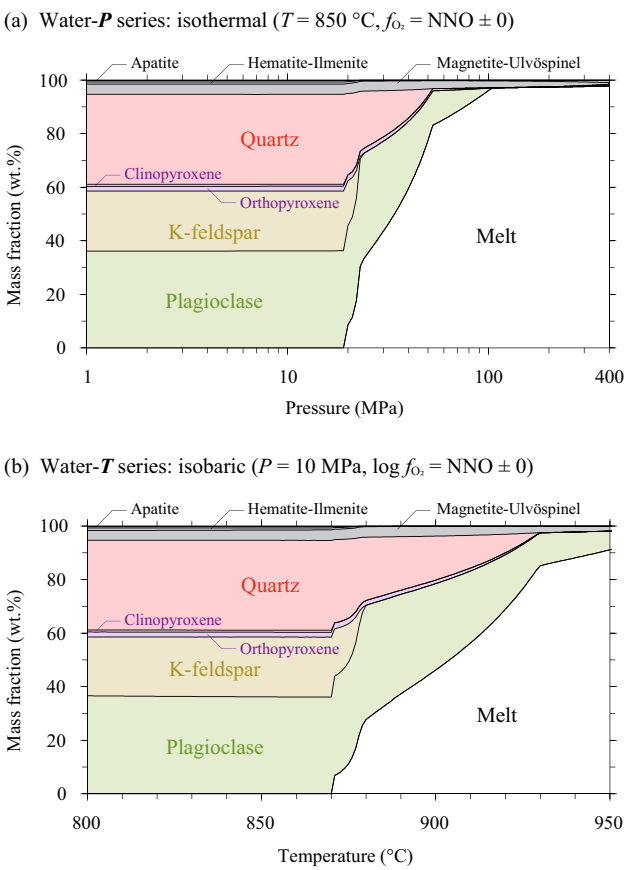

Fig. 12 Mass fractions of phases for a melt composition of the SAK-W glass in equilibrium **a** at 1–400 MPa and 850 °C, and **b** at 10 MPa and 800–950 °C calculated using the rhyolite-MELTS software (Gualda et al. 2012). The oxygen fugacity was set to NNO ± 0

Given that the diktytaxitic texture was formed extensively at 850 °C and 10–20 MPa and partly at 850 °C and 40 MPa and at 900 °C and 10 MPa, we conclude that the *P*–*T* conditions for the predominant formation of diktytaxitic texture are ± ~10 MPa and ± ~20 °C within the solidus. Above these *P*–*T* conditions, the equilibrium melt fraction increases and the intersertal texture replaces the diktytaxitic texture. Below these conditions, higher undercooling triggered rapid melt crystallization into nanolites and possibly ultrananolites, inhibiting evaporation in the experiments. Notably, undercooling would be much smaller in slow-cooling natural magmas than that in the present experiments. Thus, nanolite crystallization is hindered, and a diktytaxitic texture is formed at a lower temperature.

Implications for volcanology

Diktytaxitic texture as an indicator of magma emplacement conditions and source environments of volcanic pyroclasts

Diktytaxitic groundmass and vapor-phase silica deposits typically occur in lava domes and necks (e.g., Pallister et al. 2008; Závada et al. 2015) and block and ash flows originating from lava domes (e.g., Horwell et al. 2013; Kushnir et al. 2016; Schipper et al. 2017; Ikegami et al. 2018). The results of the present experiments provide quantitative constraints on emplacement conditions. They are also common in volcanic ash from Vulcanian explosions (e.g., Gaunt et al. 2016). These ashes were derived from shallow-intruded lava plugs near the solidus temperature (Diller et al. 2006), and the residence time under these conditions was constrained to be more than 4–8 days. The timescale for diktytaxitic texture formation is shorter than the cooling timescale of magma in lava domes and volcanic conduits, suggesting that the gap of *P*–*T* conditions from the solidus in internal lava domes or shallow-intruded lava plugs where those diktytaxitic textures formed were likely within ± ~10 MPa and ± ~20 °C.

Kushnir et al. (2016) reported the combined occurrence of diktytaxitic texture and cristobalite in the lava dome of the Merapi Volcano (Indonesia). They concluded that cristobalite was formed by gas-driven filter pressing during decompression based on the observation that they always formed at the edges of the vesicles. However, gas-driven filter pressing is not necessary for forming a diktytaxitic texture. Schipper et al. (2017) suggested that vapor-phase cristobalite can serve as a qualitative textural indicator of halogen degassing in slowly cooled volcanic rocks (e.g., lava flows and domes) on the assumption that transport via silicon halides (SiF_4 and $SiCl_4$) is necessary for its formation. However, the results of this study show that high concentrations of HF/HCl vapor are not necessary for the formation of the diktytaxitic texture and associated cristobalite. Note that our experiments prove that the melt evaporation and condensation process is effective in forming diktytaxitic textures and do not rule out the gas-driven filter pressing process or the halogen corrosion process. The diktytaxitic textures found in natural volcanic rocks may be formed concurrently by these three processes. To understand a dominant mechanism behind the formation of diktytaxitic textures, further detailed chemical investigations of both textures themselves and adjacent glasses are necessary. As shown by Yoshimura and Nakagawa (2021), the corrosion process by halogen-rich gases is most likely to be effective when the interface of the glass to the diktytaxitic void is highly Cl enriched.

Effect of the formation of diktytaxitic texture on lava dome explosivity

Horwell et al. (2013) proposed that the effect of silica mineral deposition in a lava dome on its permeability and mechanical strength depends on whether the silica is supplied by "bulk transport" from the deeper conduit or by "local redistribution" in a small area within the dome. Boudon et al. (2015) interpreted the high concentration of cristobalite in some diluted pyroclastic density currents as evidence that cristobalite has formed a "carapace" at the exterior of the lava dome. If this occurs, the permeability decreases and the strength of the lava dome increases, leading to an explosive eruption. However, Kushnir et al. (2016) indicated that the formation of a diktytaxitic texture may have a greater impact on the gas permeability of dome-forming lavas than on cristobalite deposition.

The present experiments revealed that the formation of diktytaxitic texture and vapor-phase minerals resulted from the selection of the fastest crystallization pathway with the lowest activation energy. Because the diktytaxitic texture is a fine structure with a small aperture size and high pore tortuosity, the gas-flow rate through the pores is expected to be small, and hence, there must be numerous heterogeneous nucleation sites and sufficient time for deposition. Therefore, water vapor is unlikely to become highly supersaturated with the melt components without immediate deposition. Considering these reaction kinetics, a significant bulk transport of silica at the dome scale is unlikely. The effect of the geometric transition from spherical bubbles to interconnected diktytaxitic pores is expected to increase permeability. We point out that the diktytaxitic texture is formed pervasively in the magmas in contrast to local structures such as tuffisite veins. Even though the absolute value of the permeability of the diktytaxitic texture is small, its contribution to outgassing, and thus, preventing lava dome explosions, can be significant.

Conclusions

The formation of diktytaxitic groundmass texture and vapor-phase cristobalite deposition, as found in natural lava dome rocks and volcanic ashes, were simulated through isothermal-isobaric crystallization experiments of pumices with rhyolitic glass under water-saturated conditions. In the near-solidus conditions (± ~10 MPa and ± ~20 °C within the solidus; 10–20 MPa and 850 °C for the present starting material), the interstitial glass was found to be almost consumed in 189 h as a result of evaporation and deposition of cristobalite and alkali feldspar, followed by albite-rich

plagioclase from the melt. Because halogens are not required for this evaporation–deposition process, the occurrence of diktytaxitic textures does not necessarily indicate the presence of halogen-rich volcanic gases. The occurrence of a diktytaxitic texture and vapor-phase cristobalite is useful for constraining the *P*–*T* conditions of the source region of volcanic pyroclasts and the emplacement conditions of lava domes and shallow intrusion. The deposition of residual melt and vapor-phase crystals is the process of late-stage magma crystallization before silicic magmas are exposed to the ground surface. The structural transition of bubbles with low connectivity to the highly interconnected diktytaxitic pores in the microlite interstices may allow the pervasive outgassing from the interior of the lava dome.

Supplementary Information The online version contains supplementary material available at https://doi.org/10.1007/s00410-024-02105-4.

Acknowledgements We thank M. Nemoto for providing technical assistance with the micro-Raman spectroscopic measurements. This work was supported by JSPS KAKENHI grants 22KJ0568 to RS, 16H06348 and 22H00162 to MN, and 18H01296 to SO, and by the Ministry of Education, Culture, Sports, Science and Technology (MEXT) of Japan through its "Integrated Program for Next Generation Volcano Research and Human Resource Development" and "Earthquake and Volcano Hazards Observation and Research Program" to MN.

Author contributions Ryosuke Sakurai: Conceptualization, experimental investigation, data acquisition, validation, writing—original draft, funding acquisition; Michihiko Nakamura: Supervision, writing—review and major editing, funding acquisition; Satoshi Okumura: Technical support for hydrothermal experiments, writing—review and minor editing, funding acquisition; Mayumi Mujin: Technical support for SEM–EDS, writing—review and minor editing; Takayuki Nakatani: Technical support for Raman spectroscopy, writing—review and minor editing.

Funding Open Access funding provided by The University of Tokyo.

Data availability Data are available through UTokyo Repository at https://doi.org/10.15083/0002008069.

Declarations

Conflict of interest The authors declare that they have no known competing financial interests or personal relationships that could have appeared to influence the work reported in this paper.

References

Anderson AT Jr, Swihart GH, Artioli G, Geiger CA (1984) Segregation vesicles, gas filter-pressing, and igneous differentiation. J Geol 92:55–72. https://doi.org/10.1086/628834

Bacon CR (1986) Magmatic inclusions in silicic and intermediate volcanic rocks. J Geophys Res Solid Earth 10:6091–6112. https://doi.org/10.1029/JB091iB06p06091

Baxter PJ, Bonadonna C, Dupree R, Hards VL, Kohn SC, Murphy MD, Nichols A, Nicholson RA, Norton G, Searl A, Sparks RSJ, Vickers BP (1999) Cristobalite in volcanic ash of the Soufriere Hills Volcano, Montserrat, British West Indies. Science 283:1142–1145. https://doi.org/10.1126/science.283.5405.1142

Blundy J, Cashman K (2001) Ascent-driven crystallisation of dacite magmas at Mount St Helens, 1980–1986. Contrib Mineral Petrol 140:631–650. https://doi.org/10.1007/s004100000219

Boudon G, Balcone-Boissard H, Villemant B, Morgan DJ (2015) What factors control superficial lava dome explosivity? Sci Rep 5:14551. https://doi.org/10.1038/srep14551

Carpenter MA, Salje EK, Graeme-Barber A (1998) Spontaneous strain as a determinant of thermodynamic properties for phase transitions in minerals. Eur J Mineral 10:621–691. https://doi.org/10.1127/ejm/10/4/0621

Cassidy M, Manga M, Cashman K, Bachmann O (2018) Controls on explosive-effusive volcanic eruption styles. Nat Commun 9:2839. https://doi.org/10.1038/s41467-018-05293-3

Chao CH, Lu HY (2002) β-Cristobalite stabilization in (Na_2O + Al_2O_3)-added silica. Metall Mater Trans A 33:2703–2711. https://doi.org/10.1007/s11661-002-0392-y

Damby DE, Llewellin EW, Horwell CJ, Williamson BJ, Najorka J, Cressey G, Carpenter M (2014) The α–β phase transition in volcanic cristobalite. J Appl Crystallogr 47:1205–1215. https://doi.org/10.1107/S160057671401070X

Daniel I, Gillet PH, McMillan PF, Richet P (1995) An in-situ high-temperature structural study of stable and metastable $CaAl_2Si_2O_8$ polymorphs. Mineral Mag 59:25–33. https://doi.org/10.1180/minmag.1995.59.394.03

Dapiaggi M, Pagliari L, Pavese A, Sciascia L, Merli M, Francescon F (2015) The formation of silica high temperature polymorphs from quartz: influence of grain size and mineralising agents. J Eur Ceram Soc 35:4547–4555. https://doi.org/10.1016/j.jeurceramsoc.2015.08.015

De Hoog JC, Van Bergen MJ, Jacobs MH (2005) Vapour-phase crystallisation of silica from SiF_4-bearing volcanic gases. Ann Geophys 48:775–785. https://doi.org/10.4401/ag-3233

Deer WA, Howie RA, Zussman J (2013) An introduction to the rock-forming minerals, 3rd edn. Berforts Information Press, Hertfordshire. https://doi.org/10.1180/DHZ

Diller K, Clarke AB, Voight B, Neri A (2006) Mechanisms of conduit plug formation: implications for vulcanian explosions. Geophys Res Lett 33:L20302. https://doi.org/10.1029/2006GL027391

Fabel GW, White WB, White EW, Roy R (1972) Structure of lunar glasses by Raman and soft X-ray spectroscopy. Proc Third Lunar Sci Conf, Geochim Cosmochim Acta Suppl 3:939–951

Freeman JJ, Wang A, Kuebler KE, Jolliff BL, Haskin LA (2008) Characterization of natural feldspars by Raman spectroscopy for future planetary exploration. Can Mineral 46:1477–1500. https://doi.org/10.3749/canmin.46.6.1477

Fuller RE (1931) The geomorphology and volcanic sequence of Steens Mountain in southeastern Oregon. Univ Wash Pub Geol 3:1–30

Gaunt HE, Bernard B, Hidalgo S, Proaño A, Wright H, Mothes P, Criollo E, Kueppers U (2016) Juvenile magma recognition and eruptive dynamics inferred from the analysis of ash time series: the 2015 reawakening of Cotopaxi volcano. J Volcanol Geotherm Res 328:134–146. https://doi.org/10.1016/j.jvolgeores.2016.10.013

Gillet P, Le Cléac'h A, Madon M (1990) High-temperature Raman spectroscopy of SiO_2 and GeO_2 polymorphs: anharmonicity and thermodynamic properties at high-temperatures. J Geophys Res Solid Earth 95:21635–21655. https://doi.org/10.1029/JB095iB13p21635

Gin S, Delaye JM, Angeli F, Schuller S (2021) Aqueous alteration of silicate glass: state of knowledge and perspectives. NPJ Mater Degrad 5:42. https://doi.org/10.1038/s41529-021-00190-5

Goff F (1996) Vesicle cylinders in vapor-differentiated basalt flows. J Volcanol Geotherm Res 71:167–185. https://doi.org/10.1016/0377-0273(95)00073-9

Gualda GA, Ghiorso MS, Lemons RV, Carley TL (2012) Rhyolite-MELTS: a modified calibration of MELTS optimized for silica-rich, fluid-bearing magmatic systems. J Petrol 53:875–890. https://doi.org/10.1093/petrology/egr080

Hashimoto A (1992) The effect of H_2O gas on volatilities of planet-forming major elements: I. Experimental determination of thermodynamic properties of Ca-, Al-, and Si-hydroxide gas molecules and its application to the solar nebula. Geochim Cosmochim Acta 56:511–532. https://doi.org/10.1016/0016-7037(92)90148-C

Higuchi K, Koriyama C, Akiba S (2012) Increased mortality of respiratory diseases, including lung cancer, in the area with large amount of ashfall from Mount Sakurajima Volcano. J Environ Public Health 2012:257831. https://doi.org/10.1155/2012/257831

Hillman SE, Horwell CJ, Densmore AL, Damby DE, Fubini B, Ishimine Y, Tomatis M (2012) Sakurajima volcano: a physico-chemical study of the health consequences of long-term exposure to volcanic ash. Bull Volcanol 74:913–930. https://doi.org/10.1007/s00445-012-0575-3

Horwell CJ, Sparks RSJ, Brewer TS, Llewellin EW, Williamson BJ (2003) Characterization of respirable volcanic ash from the Soufrière Hills volcano, Montserrat, with implications for human health hazards. Bull Volcanol 65:346–362. https://doi.org/10.1007/s00445-002-0266-6

Horwell CJ, Williamson BJ, Llewellin EW, Damby DE, Le Blond JS (2013) The nature and formation of cristobalite at the Soufrière Hills volcano, Montserrat: implications for the petrology and stability of silicic lava domes. Bull Volcanol 75:696. https://doi.org/10.1007/s00445-013-0696-3

Ikegami F, McPhie J, Carey R, Mundana R, Soule A, Jutzeler M (2018) The eruption of submarine rhyolite lavas and domes in the deep ocean–Havre 2012. Kermadec Arc Front Earth Sci 6:147. https://doi.org/10.3389/feart.2018.00147

Kingma KJ, Hemley RJ (1994) Raman spectroscopic study of microcrystalline silica. Am Mineral 79:269–273

Kushnir AR, Martel C, Bourdier JL, Heap MJ, Reuschlé T, Erdmann S, Komorowski JC, Cholik N (2016) Probing permeability and microstructure: unravelling the role of a low-permeability dome on the explosivity of Merapi (Indonesia). J Volcanol Geotherm Res 316:56–71. https://doi.org/10.1016/j.jvolgeores.2016.02.012

Lafuente B, Downs RT, Yang H, Stone N (2015) The power of databases: the RRUFF project. In: Armbruster T, Danisi RM (eds) Highlights in mineralogical crystallography. De Gruyter, Berlin, pp 1–30. https://doi.org/10.1515/9783110417104-003

Liang JJ, Lin QH, Zhang X, Jin T, Zhou YZ, Sun XF, Choi BG, Kim IS, Do JH, Jo CY (2017) Effects of alumina on cristobalite crystallization and properties of silica-based ceramic cores. J Mater Sci Technol 33:204–209. https://doi.org/10.1016/j.jmst.2016.02.012

Martel C, Pichavant M, Di Carlo I, Champallier R, Wille G, Castro JM, Devineau K, Davydova VO, Kushnir AR (2021) Experimental constraints on the crystallization of silica phases in silicic magmas. J Petrol 62:egab004. https://doi.org/10.1093/petrology/egab004

Matsumoto A, Nakagawa M, Amma-Miyasaka M, Iguchi M (2013) Temporal variations of the petrological features of the juvenile materials during 2006 to 2010 from Showa Crater, Sakurajima Volcano, Kyushu, Japan. Bull Volcan Soc Japan 58:191–212. https://doi.org/10.18940/kazan.58.1_191

Mujin M, Nakamura M, Miyake A (2017) Eruption style and crystal size distributions: crystallization of groundmass nanolites in the 2011 Shinmoedake eruption. Am Mineral 102:2367–2380. https://doi.org/10.2138/am-2017-6052CCBYNCND

Nekvasil H, Burnham CW (1987) The calculated individual effects of pressure and water content on phase equilibria in the granite system. In: Mysen BO (ed) Magmatic processes: physicochemical principles, the geochemical society special publication no. 1. The Geochemical Society, Pennsylvania, pp 433–445

Okumura S, Ishibashi H, Itoh S, Suzumura A, Furukawa Y, Miwa T, Kagi H (2021) Decompression experiments for sulfur-bearing hydrous rhyolite magma: redox evolution during magma decompression. Am Mineral 106:216–225. https://doi.org/10.2138/am-2020-7535

Opila EJ, Fox DS, Jacobson NS (1997) Mass spectrometric identification of Si-O-H(g) species from the reaction of silica with water vapor at atmospheric pressure. J Am Ceram Soc 80:1009–1012. https://doi.org/10.1111/j.1151-2916.1997.tb02935.x

Otsuki S, Nakamura M, Okumura S, Sasaki O (2015) Interfacial tension-driven relaxation of magma foam: an experimental study. J Geophys Res Solid Earth 120:7403–7424. https://doi.org/10.1002/2015JB012391

Pallister JS, Thornber CR, Cashman KV, Clynne MA, Lowers H, Mandeville CW, Brownfield IK, Meeker GP (2008) Petrology of the 2004–2006 Mount St. Helens lava dome-implications for magmatic plumbing and eruption triggering. US Geol Surv Prof Pap 1750:647–702. https://doi.org/10.3133/pp175030

Peck DL (1978) Cooling and vesiculation of Alae lava lake, Hawaii. USGS Prof Paper 935-B, 59 pp. https://doi.org/10.3133/pp935B

Pistone M, Arzilli F, Dobson KJ, Cordonnier B, Reusser E, Ulmer P, Marone F, Whittington AG, Mancini L, Fife JL, Blundy JD (2015) Gas-driven filter pressing in magmas: insights into in-situ melt segregation from crystal mushes. Geology 43:699–702. https://doi.org/10.1130/G36766.1

Pistone M, Baumgartner LP, Bégué F, Jarvis PA, Bloch E, Robyr M, Müntener O, Sisson TW, Blundy JD (2020) Felsic melt and gas mobilization during magma solidification: an experimental study at 1.1 kbar. Front Earth Sci 8:175. https://doi.org/10.3389/feart.2020.00175

Plyasunov AV (2011) Thermodynamic properties of H_4SiO_4 in the ideal gas state as evaluated from experimental data. Geochim Cosmochim Acta 75:3853–3865. https://doi.org/10.1016/j.gca.2011.04.016

Plyasunov AV (2012) Thermodynamics of $Si(OH)_4$ in the vapor phase of water: Henry's and vapor–liquid distribution constants, fugacity and cross virial coefficients. Geochim Cosmochim Acta 77:215–231. https://doi.org/10.1016/j.gca.2011.11.019

Sanders IS (1986) Gas filter-pressing origin for segregation vesicles in dykes. Geol Mag 123:67–72. https://doi.org/10.1017/S0016756800026546

Sato T, Shimosato T, Klinman DM (2018) Silicosis and lung cancer: current perspectives. Lung Cancer Targets Therapy 9:91. https://doi.org/10.2147/lctt.s156376

Schipper CI, Castro JM, Tuffen H, Wadsworth FB, Chappell D, Pantoja AE, Simpson MP, Le Ru EC (2015) Cristobalite in the 2011–2012 Cordón Caulle eruption (Chile). Bull Volcanol 77:34. https://doi.org/10.1007/s00445-015-0925-z

Schipper CI, Mandon C, Maksimenko A, Castro JM, Conway CE, Hauer P, Kirilova M, Kilgour G (2017) Vapor-phase cristobalite as a durable indicator of magmatic pore structure and halogen degassing: an example from White Island volcano (New Zealand). Bull Volcanol 79:74. https://doi.org/10.1007/s00445-017-1157-1

Schipper CI, Castro JM, Kennedy BM, Christenson BW, Aiuppa A, Alloway B, Forte P, Tuffen H (2019) Halogen (Cl, F) and sulphur release during explosive, effusive, and intrusive phases of the 2011 rhyolitic

eruption at Cordón Caulle volcano (Chile). Volcanica 2:73–90. https://doi.org/10.30909/vol.02.01.7390

Schipper CI, Rickard WDA, Reddy SM, Saxey DW, Castro JM, Fougerouse D, Quadir Z, Conway C, Prior DJ, Lilly K (2020) Volcanic SiO_2-cristobalite: a natural product of chemical vapor deposition. Am Mineral 105:510–524. https://doi.org/10.2138/am-2020-7236

Sisson TW, Bacon CR (1999) Gas-driven filter pressing in magmas. Geology 27:613–616. https://doi.org/10.1130/0091-7613(1999)027%3c0613:GDFPIM%3e2.3.CO;2

Sparks RSJ (1997) Causes and consequences of pressurisation in lava dome eruptions. Earth Planet Sci Lett 150:177–189. https://doi.org/10.1016/S0012-821X(97)00109-X

Wen S, Nekvasil H (1994) SOLVALC: an interactive graphics program package for calculating the ternary feldspar solvus and for two-feldspar geothermometry. Comput Geosci 20:1025–1040. https://doi.org/10.1016/0098-3004(94)90039-6

Yoshimura S, Nakagawa M (2021) Chlorine heterogeneity in volcanic glass as a faithful record of silicic magma degassing. J Geophys Res Solid Earth 126:e2020JB021195. https://doi.org/10.1029/2020JB021195

Závada P, Dědeček P, Lexa J, Keller GR (2015) Devils Tower (Wyoming, USA): a lava coulée emplaced into a maar-diatreme volcano? Geosphere 11:354–375. https://doi.org/10.1130/GES01166.1